Nanoscale Phononic Analog of the Ranque-Hilsch Vortex Tube

Leonardo Medrano Sandonas[1,2,*] Álvaro Rodríguez Méndez,[1] Rafael Gutierrez[1,†]
Gianaurelio Cuniberti[1,3,4] and Vladimiro Mujica[5,6]

[1]*Institute for Materials Science and Max Bergmann Center of Biomaterials, TU Dresden, Dresden 01062,
Germany*

[2]*Department of Physics and Materials Science, University of Luxembourg, Luxembourg L-1511, Luxembourg*

[3]*Center for Advancing Electronics Dresden, TU Dresden, Dresden 01062, Germany*

[4]*Dresden Center for Computational Materials Science (DCMS), TU Dresden, Dresden 01062, Germany*

[5]*School of Molecular Sciences, Arizona State University, Tempe, Arizona 85287, USA*

[6]*Kimika Fakultatea, Euskal Herriko Unibertsitatea and Donostia International Physics Center (DIPC),
P. K. 1072, Donostia, Euskadi 20080, Spain*

Thermal management is a current global challenge that must be addressed exhaustively. We propose the design of a nanoscale phononic analog of the Ranque-Hilsch vortex tube in which heat flowing at a given temperature is split into two different streams going to the two ends of the device, inducing a temperature asymmetry. Our nanoscale prototype consists of two carbon nanotubes (capped and open) connected by molecular chains. The results show that the structural asymmetry in the contact regions is the key factor for producing the flux asymmetry and, hence, the induced temperature-bias effect. The effect can be controlled by tuning the thermal-equilibration temperature, the number of chains, and the chain length. Deposition on a substrate adds another variable to the manipulation of the flux asymmetry but the effect vanishes at very large substrate temperatures. Our study yields insights into the thermal management in nanoscale materials, especially the crucial issue of whether the thermal asymmetry can survive phonon scattering over relatively long distances, and thus provides a starting point for the design of a nanoscale phononic analog of the Ranque-Hilsch vortex tube.

I. INTRODUCTION

Gaining control over heat flow at the nanoscale poses a major challenge to current experimental techniques. The issue here is not only the reduction of heat dissipation in nanoelectronic devices or the blocking of thermal transport to increase the thermoelectric efficiency [1,2], but also to engineer thermal devices to exploit the richness of nanoscale material properties [3–7]. Thus, analogs of electronic devices, such as thermal rectifiers, thermal transistors, and thermal logic gates, have already been theoretically proposed and in a few cases experimentally demonstrated [8–21]. More recent developments involve the design of thermal clocks and of phononic metamaterials and phononic filters [5,22–28]. A deeper understanding of the underlying nanoscale physical processes mediating such effects has been gained by combining a variety of computational tools based on both classical-mechanics approaches and quantum mechanical methodologies (for

recent reviews of this topic, see Refs. [29,30]). In particular, simulations based on nonequilibrium atomistic molecular dynamics (NEMD) have proven to be a very versatile computational approach, naturally including anharmonic effects through appropriate force fields, thus allowing for the description of physical effects, e.g., thermal rectification, thermoelectricity, and interface thermal conduction, where the nonlinearity of the atomic vibrations plays a crucial role [9,10,31,32].

Concerning the variables that can be used for tuning nanoscale thermal transport in phononic devices, there are two major parameters that have turned out to be crucial: (i) structural asymmetry, either at the interface to the thermal baths or intrinsic to the materials used as thermal devices [33–39]; and (ii) substrate deposition [40–45]. For instance, the outer and inner atomic conformations of two-dimensional (2D) materials have been engineered in order to control the heat-flux intensity and direction, improving their performance as thermal rectifiers [36,37, 46]. The arrangement of 2D materials into planar and out-of-plane heterostructures has recently attracted considerable attention due to the possibility of manipulating

---

*leonardo.medrano@uni.lu
†rafael.gutierrez@tu-dresden.de

034008-1

the interface thermal conductance. It has been demonstrated that substrate deposition could help to intensify or reduce the thermal-rectification effect in 2D heterojunctions [45], via the modification of the out-of-plane modes of the heat sources at low frequencies. Because of their high thermal conductivity, which is dependent on several atomic features (e.g., length, diameter, and chirality), carbon nanotubes (CNT) have been also extensively investigated as potential materials for phononic devices [47] and even three-dimensional graphene-nanotube networks have already been proposed [48,49]. Additionally, the design of the organic-inorganic materials interface has revolutionized the field of nanoscale thermal transport in recent years. This has been, in particular, the case for developing molecular thermoelectrics and phononic filters, in which organic materials could be used as a thermal modulator via molecular functionalization or by bridging inorganic materials [1,28,50–52]. Although these experimental and computational studies have contributed considerably to gaining a deeper understanding of thermal transport in nanoscale materials, there still is, however, the challenge of designing phononic devices for the adequate management of thermal energy at different length scales.

In the current investigation, we propose a nanoscale phononic analog of the Ranque-Hilsch vortex tube [53,54], where a gas flowing at a given temperature is split into two streams at different temperatures. It has been possible to fabricate that device during the past century without violating the laws of thermodynamics and it has been used for, e.g., train refrigeration [55]. Our proposed setup operates as a true energy-splitting nanodevice by exploiting selective filtering at strongly asymmetric interfaces, relying on a physical principle similar to that of our recently proposed molecular-based phononic filter device [28]: however, the working mechanism is different. Thus, unlike a thermal rectifier, where the temperature bias is applied between two thermal baths (two carbon nanotubes in our case study), the two different temperatures in the baths of the phononic Ranque-Hilsch tube are induced by only heating a central region that bridges the two nanotubes and that is coupled to the baths by strongly structurally asymmetric interfaces. In Sec. II, we describe the design of the phononic Ranque-Hilsch tube in more detail and then we proceed to discuss the results concerning the working mechanism of the device for the free-standing and suspended cases.

II. COMPUTATIONAL MODEL

An atomistic representation of the two-terminal nanoscale device that we are envisioning is shown in Fig. 1(a). The system consists of two semi-infinite (5,5) carbon nanotubes, between which one or a few benzene chains with varying numbers of monomers are sandwiched. To increase the device structural asymmetry, the end of one of the nanotubes (the left one in the figure) is
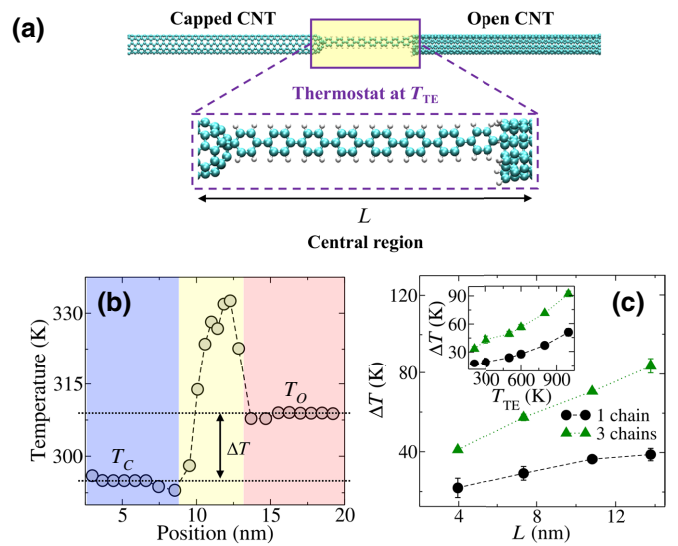

FIG. 1.   (a) A schematic representation of the target molecular junctions in the present study. A molecular system is connected to two different carbon nanotubes, capped and open nanotubes. (b) The temperature profile of the complete system after reaching thermal equilibrium for $T_{TE} = 300$ K. Here, a temperature bias $\Delta T = T_C - T_O$ is induced by action of the thermostat in the central region. (c) The variation of the induced temperature bias ΔT as a function of the length of the central region for one and three chains of benzene monomers, at 800 K, which is the thermal-equilibration temperature in the central bath. The inset shows the temperature dependence of ΔT for one and three chains of 24 benzene monomers.

capped with half of a C_{60} fullerene, while the end of the other one is left open. This justifies the specific choice of a (5,5) nanotube, since it allows a perfect matching of the fullerene cap to the nanotube open end. As shown below (see also Fig. S1 of the Supplemental Material [56]), this structural asymmetry is an essential ingredient in order to obtain an induced temperature bias (ITB) in the device.

For the thermal equilibration of the central device region, which includes the molecular chain as well as part of the nanotubes [see the enclosed region in Fig. 1(a)], at a temperature T_{TE}, an *NVT* ensemble is considered, using a Nosé-Hoover thermostat with a relaxation time of 0.1 ps. The equilibrium molecular-dynamics (MD) simulations are carried out by using the LAMMPS code [57], with interactions among the C and H atoms described using the AIREBO force field [58]. The velocity Verlet algorithm is used to integrate Newton's equations of motion and the MD time step is set to 0.1 fs. All investigated structures are initially relaxed using the quickstep method. For each given T_{TE}, a temperature-equilibration simulation is run for 6 ns and time averages of the temperature and heat current are carried out over the last nanosecond of the simulation. The temperature profile is then computed by dividing the system into a number of slabs and using the relation

$T_i = (1/3 N_i k_B) \sum_{k=1}^{N_i} m_k v_k^2$, where N_i is the number of atoms in the ith slab and m_k and v_k correspond to the atomic mass and velocity of atom number k, respectively. Additional simulations considering the Langevin thermostat are also performed to demonstrate the influence of the heat-bath model on the physical effects reported in this work [59,60]. To avoid spurious effects related to the specific choice of initial velocities, an average over five random choices of the initial velocity distribution is additionally performed.

Our model clearly assumes that the mechanism for heat transport is exclusively related to phonon transport. Also, since our model is based on classical transport equations, a quantum study of phonon scattering is not included. A similar limitation holds for the inclusion of electron-phonon interactions. It is worth noting that even with these constraints, we are able to study and predict the asymmetric thermal behavior of complex nanojunctions [7].

III. RESULTS AND DISCUSSION

Figure 1(b) displays a central result of this study. Upon reaching thermal equilibrium, a nonhomogeneous stationary temperature profile is established in the central region and, more importantly, an induced temperature bias $\Delta T = T_O - T_C$ sets in between the left (temperature T_C) and right (temperature T_O) nanotubes, the capped tube displaying the lower temperature. As shown in Fig. 1(c), the ITB scales approximately linearly with the length of the molecular chain bridging the nanotubes and its slope becomes larger when the number of molecular chains attached in parallel between the nanotubes increases from one to three. Further, for a given length of approximately 10.8 nm, ΔT gets larger after increasing the temperature T_{TE} of the central region [see the inset of Fig. 1(c)]. The existence of the ITB and its linear dependence with respect to T_{TE} are also observed by using the Langevin thermostat as a heat bath in the central region (see Fig. 5 in the Appendix).

A question naturally arises: What is the mechanism behind this thermal asymmetry? To answer this question, we compute the heat flux per atom J into each nanotube (regions RA and RB in the top panel of Fig. 2), according to the relation [61] $\mathbf{J} = (1/NV) \left[\sum_i e_i \mathbf{v}_i + \sum_i \mathbf{Q}_i \cdot \mathbf{v}_i \right]$, where N is the number of atoms in selected region, V is the volume of the simulation domain, $\mathbf{v}_i$ denotes the velocity vector, e_i is the per-atom total energy (kinetic and potential), and $\mathbf{Q}_i$ is the per-atom stress tensor. The sum goes through all the atoms inside the selected region. Similar to ΔT, the flux J is calculated by averaging over five different initial-velocity configurations. The computed heat flux per atom as a function of the thermal-equilibration temperature T_{TE}, shown in the bottom panel of Fig. 2, displays some interesting features: first, the flux into the open-ended nanotube is always larger than the one into the capped
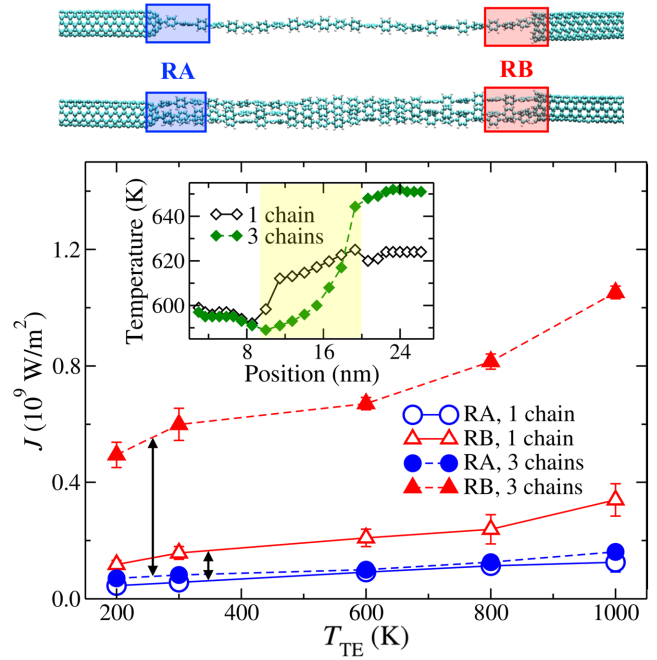

FIG. 2. The heat flux per atom as a function of the thermal-equilibration temperature T_{TE} in the central bath for the regions RA and RB highlighted in the top panel. We show results for one and three molecular chains interconnecting the nanotubes, each consisting of 24 benzene monomers. The increased flux asymmetry with an increasing number of chains correlates with a similar increase in the induced temperature bias shown in Fig. 1(c). Note also the weak dependence of the flux into the capped nanotube on the number of molecular chains. On the contrary, the flux increases strongly when going from one to three chains in the case of the open-ended nanotube. The inset shows the temperature profile for one and three chains at an thermal-equilibration temperature $T_{TE} = 600$ K. The weak dependence of the flux into the RA region is reflected into a small change in the steady-state temperature T_C in that region.

region; second, it is evident that with only one molecular chain bridging the two nanotubes, the flux asymmetry is relatively small (highlighted by the arrows). Finally, increasing the number of molecular chains does not appreciably affect the heat flux into the capped nanotube but, rather, it leads to a stronger increase of the flux into the open-ended nanotube. This increased heat-flux asymmetry mirrors the increasing ITB with the number of chains, previously shown in Fig. 1(c). Moreover, the very weak dependence of the flux into the RA region on the number of molecular chains explains the small variation of the steady-state temperature T_C of the capped CNT after increasing the number of chains (see the inset of Fig. 2). This can be better understood by analyzing the average strength of the bonds in regions RA and RB. Thus, we compute $D_{i-j} = \text{Trace}[\mathrm{K}_{i-j} (\mathrm{K}^T)_{i-j}]$ which gives information on the bond strength for each atomic pair (i, j) [62]. Here, the indices i, j denote neighboring atoms in the

corresponding regions. The real number D_{i-j} is obtained by using the 3×3 submatrix K_{i-j} associated with the force constants of atoms i and j. The total force-constant matrix K is obtained by using the density-functional tight-binding method as implemented in the DFTB+ code [63]. The average strength of the bonds is then defined as $\langle D \rangle_X = (1/N_{\text{bond}}) \sum_{i,j \in X} D_{i-j}$, where X refers to RA or RB, and N_{bond} is the number of bonds in the corresponding region. Indeed, we find that, independently of the thermal-equilibration temperature T_{TE} and the number of chains, $\langle D \rangle_{\text{RB}}$ is always larger than $\langle D \rangle_{\text{RA}}$ and, for the junction with three molecular chains, we have $\langle D \rangle_{\text{RA}} = 0.07$ a.u. and $\langle D \rangle_{\text{RB}} = 0.15$ a.u. at $T_{\text{TE}} = 300$ K. This means that region RB allows a larger heat transfer between the molecular chains and the open-ended nanotube, which prompts a higher steady temperature in comparison to the capped nanotube. It is worth mentioning that the difference in $\langle D \rangle$ between these two regions decreases with the number of chains, which is in agreement with the reduction in ITB [see Fig. 1(c)].

The increase of ΔT can also be understood from a different perspective by looking at the phonon density of states $S(\omega)$ projected onto the regions RA and RB. $S(\omega)$ is calculated as the Fourier transform of the velocity autocorrelation function $f(t)$ and it is given by [11,45]

$$S(\omega) = \frac{1}{\text{NT}} \int f(t) \cos \omega t \, dt, \qquad (1)$$

where $f(t) = \langle \sum_{i=1}^{N} \mathbf{v_i}(t_0) \cdot \mathbf{v_i}(t) \rangle / \langle \sum_{i=1}^{N} \mathbf{v_i^2}(t_0) \rangle$. N and T are the number of atoms and the average steady-state temperature of the region of interest, respectively. To smooth the function, $S(\omega)$ is averaged over ten different time intervals after reaching the steady state. We define the parameter Φ to quantify the effect of the thermal-equilibration temperature on the phonon density of states as follows:

$$\Phi(T) = \int_0^{\omega_c(T_{\text{TE}})} \frac{S_{\text{RB}}(\omega) - S_{\text{RA}}(\omega)}{S_{\text{RB}}(\omega) + S_{\text{RA}}(\omega)} d\omega. \qquad (2)$$

Here, $S_{\text{RA/RB}}(\omega)$ is the projected phonon density of states onto region RA or RB and $\omega_c(T_{\text{TE}})$ is a (temperature-dependent) frequency cutoff that defines the upper limit of the thermally active vibrational spectral range for each given bath temperature T_{TE} (the values are listed in Table S1 of the Supplemental Material [56]). The parameter Φ is thus a global measure of the spectral asymmetry of the left and right regions and its temperature dependence for a junction with three molecular chains composed of 24 benzene monomers (approximately 10.8 nm) is displayed in Fig. 3. As becomes clear from the figure, Φ increases linearly with temperature, but it will saturate above roughly 1000 K. The increase with temperature is a measure of the increasing asymmetry in the projected spectral densities on regions RA and RB [see, e.g., $S(\omega)$ for both regions at 300
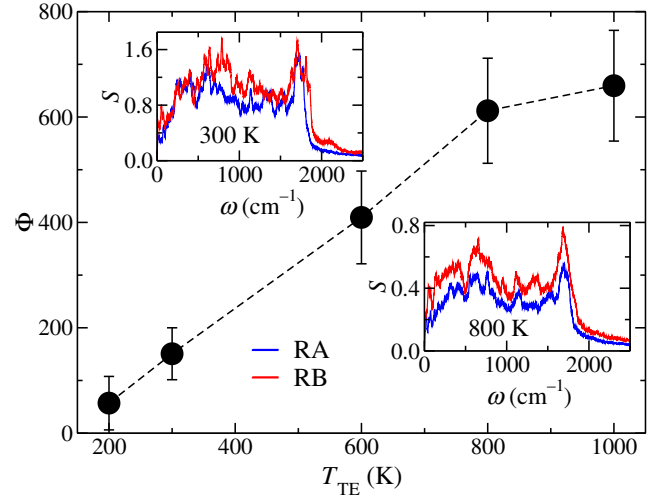

FIG. 3. The dependence of the parameter Φ [see Eq. (2)] on the thermal-equilibration temperature T_{TE} for a junction with three molecular chains composed of 24 benzene monomers each. The increase of Φ with the temperature is a fingerprint of the increased asymmetry in the spectral densities and hence of the heat flux, which ultimately leads to the induced temperature bias (ITB). The inset shows the projected density of states on regions RA and RB for two selected temperatures $T_{\text{TE}} = 300$ K and 800 K.

K and 800 K in the insets of Fig. 3], while the saturation is most likely related to the fact that once the frequency cutoff $\omega_c(T_{\text{TE}})$ becomes large enough, all relevant available vibrational modes will fall into the integration window. This effect correlates with the variation of the heat flux after heating up the central region (see Fig. 2).

The previously discussed setup is rather idealized, so that another question arises: How stable will the obtained ITB be in the presence of a substrate, where part of the device—a section of the left and right carbon nanotubes—is deposited? To clarify this issue, we consider the situation shown in Fig. 4(a), a junction with three molecular chains and 24 benzene monomers per chain over two substrates near the end of the nanotubes. Each of the substrates is composed of 1980 Si atoms and is oriented along the (100) direction. In these simulations, three *NVT* thermostats are acting on the whole setup, one for the junction region (as in the previous part of our study) and two for the substrate regions. The interaction among the Si atoms is described by a modified Tersoff potential [64]. The substrate temperature T_{subst} will range from 100 K to 500 K, while the thermal-equilibration temperature T_{TE} at the junction will be equal to 300 K for all cases. The van der Waals interaction between the device and the surface is modeled by a Lennard-Jones potential [65,66] (the corresponding parameters are listed in Table S2 of the Supplemental Material [56]). The distance between
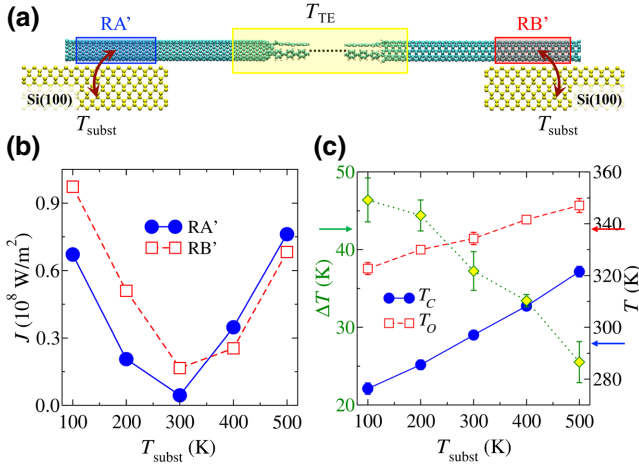
FIG. 4.   The influence of substrate deposition on the ITB effect. (a) The system simulated consists on a junction with three molecular chains and 24 benzene monomers per chain over two substrates, each one composed of 1980 Si atoms and with orientation (100), near the end of the nanotubes, as depicted in the schematic. The NVT of the central region is kept at 300 K, while the temperature of the NVT from the Si substrate is varied from 100 K to 500 K. (b) The variation of the heat flux as a function of the substrate temperature T_{subst} for the sections of nanotube that are in contact with the substrate (RA' for the capped side and RB' for the open side). The minimum of the heat flux is found when the temperatures of the thermal bath of the central region and the substrates are the same. (c) The T_{subst} dependence of the nanotube temperatures (T_C and T_O for the capped and open nanotube, respectively) and the induced temperature bias ΔT. Here, ΔT is reduced at almost half of the temperature bias without a substrate when the temperature of the substrate is at 500 K. The arrows on the left-hand and right-hand sides of the graph indicate the respective values for the free-standing system.

the junction and the substrate after geometric optimization is 2.97 Å. The simulation runs for 10 ns and then the temperature profiles and heat fluxes are computed.

The first substantial effect of the substrate on the thermal properties of the phononic Ranque-Hilsch vortex tube is reduction of the heat flux when the three NVT thermostats are at 300 K [see Fig. 4(b)]. Despite there being different regions in which the heat flux is computed compared to the free-standing case [see regions RA' and RB' in Fig. 4(a)], we find that the heat flux flowing into both nanotubes is largely reduced and that its magnitude depends on the substrate temperature T_{subst}. In fact, the dependence of the heat flux in both nanotubes with respect to T_{subst} displays a minimum around the thermal-equilibration temperature of the junction region ($T_{\text{TE}} = 300$ K). For $T_{\text{subst}} < T_{\text{TE}}$, there is a loss of heat that is going to the substrate due to the local temperature gradient, so that the temperature values for the capped (T_C) and open (T_O) nanotubes are smaller compared to those of the free-standing device [see Fig. 4(c)]. On the other hand, for $T_{\text{subst}} > T_{\text{TE}}$, the local temperature

gradient is reversed and the heat flux in region RA' will increase much faster than the corresponding one for region RB', T_O rising at a much higher speed than T_C. This phenomenon is a consequence of the stronger modification of the low-frequency modes in the capped nanotube after increasing T_{subst} (see Fig. S2 of the Supplemental Material [56]). Hence, by computing the difference between these two temperatures, we find that the ITB effect is preserved after partial deposition of the device on the silicon substrate. However, ΔT decreases as a function of the substrate temperature and, for $T_{\text{subst}} \gg T_{\text{TE}}$, the steady-state temperature of the carbon nanotubes will be dominated by the substrate temperature, wiping this effect out. In a similar way, ΔT can be also tuned by the strength of the van der Waals interaction, which opens up the possibility of additional substrate engineering of the ITB effect.

IV. CONCLUSIONS

To conclude, we demonstrate the mechanisms governing the performance of a phononic device counterpart of the Ranque-Hilsch vortex tube, which produces two different heat fluxes into the two ends of the device, inducing a nonequilibrium temperature asymmetry. The eventual technological implications of a device based on our model are highly significant for phonon-based energy and information management. Phonons are, in a certain way, interacting quasiparticles halfway between the strongly interacting electrons and the noninteracting photons. This, together with the fact that phonons can interact strongly with electrons and the possibility of including spin-dependent interactions, e.g., involving chirality, could help to define very interesting research paths.

Since structural asymmetry is found to be the essential ingredient in the design of this device, here we propose a system consisting of two (5,5)-CNT nanotubes (capped and open) connected by molecular chains made of benzene as a nanoscale prototype. Indeed, we are able to control the heat-flux asymmetry and, hence, the ITB effect in the free-standing system by tuning several factors, such as the thermal-equilibration temperature, the number of chains, and the chain length. This asymmetry is associated with the differences between the phonon density of states of the two ends of the device, which also increases as a function of the thermal-equilibration temperature. The ITB effect is also proved to be quite independent of the heat bath employed for reaching thermal equilibrium, showing the robustness of our proposed molecular device. Moreover, after depositing the nanotubes on Si(100) substrates, we can tailor the ITB effect by altering the heat flux into the nanotubes via the modification of the substrate temperature. The ITB can be canceled out at very high substrate temperatures (compared to the thermal-equilibration temperature), where the vibrational modes of the device will be governed by those from the substrates.

Clearly, additional computational studies are needed, varying the specific chemical composition of the interconnecting molecular chains as well as the type of substrate to provide a more universal picture of the demonstrated ITB effect. This is the scope of ongoing studies. We also expect that our results will encourage experimental work helping to elucidate whether the proposed phononic analog of the Ranque-Hilsch vortex tube can be successfully implemented and what the achievable sizes of the ITB are. A crucial test of our ideas is whether phonon scattering could preclude the asymmetric energy distribution, associated with the heat flow, from operating over distances that are significant in terms of the design of technologies for energy management. This is conventionally considered to be an important obstacle for the development of phononic-based technologies.

APPENDIX: INDUCED TEMPERATURE-BIAS EFFECT (ITB) BY USING LANGEVIN THERMOSTAT

As implemented in the LAMMPS code [57], the total force on each atom under the influence of the Langevin thermostat is described by $F = F_c + F_f + F_r$, where $F_f = -(m/\eta)v$ and $F_r \propto \sqrt{(k_B T m/\eta \, dt)}$. Here, F_c is the conservative force computed via the usual interparticle interactions. F_f is a frictional-drag or viscous-damping term proportional to the particle velocity v. The proportionality constant for each atom is computed as m/η, where m is the mass of the particle and η is the damping factor specified by the user. F_r is a force due to solvent atoms at a temperature T randomly bumping into the particle. In the proportionality shown above, which is derived from the fluctuation-dissipation theorem, k_B is the Boltzmann constant and dt is the time-step size. Random numbers are used to randomize the direction and magnitude of this force, as explained in Ref. [67], where a uniform random number is used (instead of a Gaussian random number) for speed.

In Figs. 5(a)–5(c), the ITB effect can still be observed by using the Langevin thermostat. The temperature bias ΔT also increases as a function of the thermal-equilibration temperature T_{TE} [see the inset of Fig. 5(b)], as it is initially found by using the Nose-Hoover thermostat. We remark that the ITB effect and the ΔT values depend on the damping parameter η (the units are picoseconds) used for the implementation of the Langevin thermostat. This parameter can be thought of as related to the viscosity of the solvent, e.g., a small value implies a higher-friction (stronger energy dissipation–energy exchange with the target system) and vice versa. Therefore, we perform an extra study to find the adequate value for our simulations. Figure 5(a) shows the variation of the temperature profile
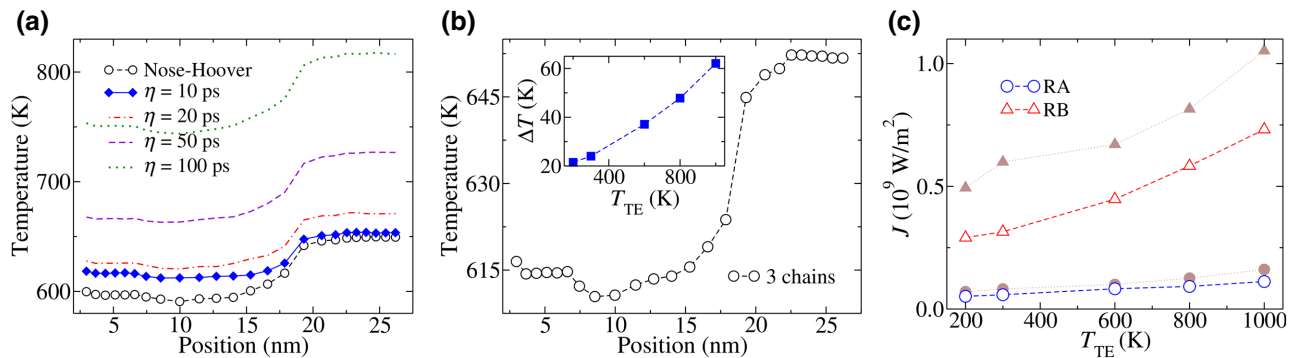

FIG. 5. A demonstration of the induced temperature-bias (ITB) effect considering the Langevin thermostat as a heat bath for a junction with three molecular chains composed of 24 benzene monomers each. (a) The variation of the temperature profile for a system equilibrated at 600 K as a function of the damping parameter η. (b) The final temperature profile of the molecular device with a thermal-equilibration temperature T_{TE} of 600 K. The inset shows the T_{TE} dependence of the induced temperature bias. (c) The heat flux per atom for regions RA (capped NT) and RB (open NT) as a function of T_{TE}. We also show the values corresponding to the Nose-Hoover thermostat (brown color). The results in panels (b) and (c) are the average over five random choices of the initial velocity distribution.

for the system equilibrated at $T_{TE} = 600$ K with respect to the damping parameter η. For all simulations, we then decide to use $\eta = 10$ ps because the obtained temperature profile is very close to that corresponding to the Nose-Hoover thermostat. The heat flux per atom is also computed by using the Langevin thermostat [see Fig. 5(c)], similar to the analysis shown in Fig. 3. The temperature dependence of the heat flux in regions RA and RB for both thermostats is the same and the values are very close. In brief, we show that the effect we are reporting is quite independent of the heat bath employed for reaching thermal equilibrium.

---

[1] A. K. Ismael and C. J. Lambert, Molecular-scale thermoelectricity: A worst-case scenario, Nanoscale Horiz. **5**, 1073 (2020).

[2] J. P. Heremans, M. S. Dresselhaus, L. E. Bell, and D. T. Morelli, When thermoelectrics reached the nanoscale, Nat. Nanotechnol. **8**, 471 (2013).

[3] N. Li, J. Ren, L. Wang, G. Zhang, P. Hänggi, and B. Li, Colloquium: Phononics: Manipulating heat flow with electronic analogs and beyond, Rev. Mod. Phys. **84**, 1045 (2012).

[4] S. Volz *et al.*, Nanophononics: State of the art and perspectives, Eur. Phys. J. B **89**, 15 (2016).

[5] I. Peralta, V. D. Fachinotti, and J. C. Álvarez Hostos, A brief review on thermal metamaterials for cloaking and heat flux manipulation, Adv. Eng. Mater. **22**, 1901034 (2020).

[6] D. Thompson, L. Zhu, E. Meyhofer, and P. Reddy, Nanoscale radiative thermal switching via multi-body effects, Nat. Nanotechnol. **15**, 99 (2020).

[7] W. Kim, R. Wang, and A. Majumdar, Nanostructuring expands thermal limits, Nano Today **2**, 40 (2007).

[8] M. Terraneo, M. Peyrard, and G. Casati, Controlling the Energy Flow in Nonlinear Lattices: A Model for a Thermal Rectifier, Phys. Rev. Lett. **88**, 094302 (2002).

[9] B. Li, J. Lan, and L. Wang, Interface Thermal Resistance between Dissimilar Anharmonic Lattices, Phys. Rev. Lett. **95**, 104302 (2005).

[10] B. Hu, L. Yang, and Y. Zhang, Asymmetric Heat Conduction in Nonlinear Lattices, Phys. Rev. Lett. **97**, 124302 (2006).

[11] J. Lee, V. Varshney, A. K. Roy, J. B. Ferguson, and B. L. Farmer, Thermal rectification in three-dimensional asymmetric nanostructure, Nano Lett. **12**, 3491 (2012).

[12] S. Pal and I. K. Puri, Thermal and gate using a monolayer graphene nanoribbon, Small **11**, 2910 (2015).

[13] V. Kubytskyi, S.-A. Biehs, and P. Ben-Abdallah, Radiative Bistability and Thermal Memory, Phys. Rev. Lett. **113**, 074301 (2014).

[14] A. Fornieri, G. Timossi, R. Bosisio, P. Solinas, and F. Giazotto, Negative differential thermal conductance and heat amplification in superconducting hybrid devices, Phys. Rev. B **93**, 134508 (2016).

[15] Q. Ruan and L. Wang, Switchability and controllability of a thermal transistor, Phys. Rev. Res. **2**, 023087 (2020).

[16] C. W. Chang, D. Okawa, A. Majumdar, and A. Zettl, Solid-state thermal rectifier, Science **314**, 1121 (2006).

[17] R. Xie, C. T. Bui, B. Varghese, Q. Zhang, C. H. Sow, B. Li, and J. T. L. Thong, An electrically tuned solid-state thermal memory based on metal-insulator transition of single-crystalline VO$_2$ nanobeams, Adv. Funct. Mater. **21**, 1602 (2011).

[18] H. Tian, D. Xie, Y. Yang, T.-L. Ren, G. Zhang, Y.-F. Wang, C.-J. Zhou, P.-G. Peng, L.-G. Wang, and L.-T. Liu, A novel solid-state thermal rectifier based on reduced graphene oxide, Sci. Rep. **2**, 523 (2012).

[19] J. Zhu, K. Hippalgaonkar, S. Shen, K. Wang, Y. Abate, S. Lee, J. Wu, X. Yin, A. Majumdar, and X. Zhang, Temperature-gated thermal rectifier for active heat flow control, Nano Lett. **14**, 4867 (2014).

[20] H. Wang, S. Hu, K. Takahashi, X. Zhang, H. Takamatsu, and J. Chen, Experimental study of thermal rectification in suspended monolayer graphene, Nat. Commun. **8**, 15843 (2017).

[21] A. M. Morsy, R. Biswas, and M. L. Povinelli, High temperature, experimental thermal memory based on optical resonances in photonic crystal slabs, APL Photonics **4**, 010804 (2019).

[22] T. Han, X. Bai, D. Gao, J. T. L. Thong, B. Li, and C.-W. Qiu, Experimental Demonstration of a Bilayer Thermal Cloak, Phys. Rev. Lett. **112**, 054302 (2014).

[23] T. Han, X. Bai, J. T. L. Thong, B. Li, and C.-W. Qiu, Full control and manipulation of heat signatures: Cloaking, camouflage and thermal metamaterials, Adv. Mater. **26**, 1731 (2014).

[24] W.-S. Yeung, V.-P. Mai, and R.-J. Yang, Cloaking: Controlling Thermal and Hydrodynamic Fields Simultaneously, Phys. Rev. Appl. **13**, 064030 (2020).

[25] S. M. Sadat and R. Y. Wang, Colloidal nanocrystal superlattices as phononic crystals: Plane wave expansion modeling of phonon band structure, RSC Adv. **6**, 44578 (2016).

[26] S. Narayana and Y. Sato, Heat Flux Manipulation with Engineered Thermal Materials, Phys. Rev. Lett. **108**, 214303 (2012).

[27] Y. Tian, T. A. Puurtinen, Z. Geng, and I. J. Maasilta, Minimizing Coherent Thermal Conductance by Controlling the Periodicity of Two-Dimensional Phononic Crystals, Phys. Rev. Appl. **12**, 014008 (2019).

[28] L. Medrano Sandonas, A. Rodriguez Mendez, R. Gutierrez, J. M. Ugalde, V. Mujica, and G. Cuniberti, Selective transmission of phonons in molecular junctions with nanoscopic thermal baths, J. Phys. Chem. C **123**, 9680 (2019).

[29] Y. Zhou, Z. Fan, G. Qin, J.-Y. Yang, T. Ouyang, and M. Hu, Methodology perspective of computing thermal transport in low-dimensional materials and nanostructures: The old and the new, ACS Omega **3**, 3278 (2018).

[30] H. Sevinçli, S. Roche, G. Cuniberti, M. Brandbyge, R. Gutierrez, and L. Medrano Sandonas, Green function, quasi-classical Langevin and Kubo-Greenwood methods in quantum thermal transport, J. Phys.: Condens. Matter **31**, 273003 (2019).

[31] J.-H. Jiang and Y. Imry, Enhancing Thermoelectric Performance Using Nonlinear Transport Effects, Phys. Rev. Appl. **7**, 064001 (2017).

[32] R. Saito, M. Mizuno, and M. S. Dresselhaus, Ballistic and Diffusive Thermal Conductivity of Graphene, Phys. Rev. Appl. 9, 024017 (2018).

[33] B. Li, L. Wang, and G. Casati, Thermal Diode: Rectification of Heat Flux, Phys. Rev. Lett. 93, 184301 (2004).

[34] B. Liu, J. A. Baimova, C. D. Reddy, S. V. Dmitriev, W. K. Law, X. Q. Feng, and K. Zhou, Interface thermal conductance and rectification in hybrid graphene/silicene monolayer, Carbon 79, 236 (2014).

[35] X.-K. Chen, Z.-X. Xie, W.-X. Zhou, L.-M. Tang, and K.-Q. Chen, Thermal rectification and negative differential thermal resistance behaviors in graphene/hexagonal boron nitride heterojunction, Carbon 100, 492 (2016).

[36] L. Medrano Sandonas, R. Gutierrez, A. Dianat, and G. Cuniberti, Engineering thermal rectification in MoS$_2$ nanoribbons: A non-equilibrium molecular dynamics study, RSC Adv. 5, 54345 (2015).

[37] Y. Wang, A. Vallabhaneni, J. Hu, B. Qiu, Y. P. Chen, and X. Ruan, Phonon lateral confinement enables thermal rectification in asymmetric single-material nanostructures, Nano Lett. 14, 592 (2014).

[38] G. Zhang and H. Zhang, Thermal conduction and rectification in few-layer graphene Y junctions, Nanoscale 3, 4604 (2011).

[39] H. Kang, F. Yang, and J. J. Urban, Thermal rectification via heterojunctions of solid-state phase-change materials, Phys. Rev. Appl. 10, 024034 (2018).

[40] J. H. Seol, I. Jo, A. L. Moore, L. Lindsay, Z. H. Aitken, M. T. Pettes, X. Li, Z. Yao, R. Huang, D. Broido, N. Mingo, R. S. Ruoff, and L. Shi, Two-dimensional phonon transport in supported graphene, Science 328, 213 (2010).

[41] J. Chen, G. Zhang, and B. Li, Substrate coupling suppresses size dependence of thermal conductivity in supported graphene, Nanoscale 5, 532 (2013).

[42] X. Zhang, H. Bao, and M. Hu, Bilateral substrate effect on the thermal conductivity of two-dimensional silicon, Nanoscale 7, 6014 (2015).

[43] A. France-Lanord, P. Soukiassian, C. Glattli, and E. Wimmer, Thermal Transport in Supported Graphene: Substrate Effects on Collective Excitations, Phys. Rev. Appl. 7, 034030 (2017).

[44] J. Zhang, Y. Hong, M. Liu, Y. Yue, Q. Xiong, and G. Lorenzini, Molecular dynamics simulation of the interfacial thermal resistance between phosphorene and silicon substrate, Int. J. Heat Mass Tran. 104, 871 (2017).

[45] L. Medrano Sandonas, G. Cuba-Supanta, R. Gutierrez, A. Dianat, C. V. Landauro, and G. Cuniberti, Enhancement of thermal transport properties of asymmetric graphene/hBN nanoribbon heterojunctions by substrate engineering, Carbon 124, 642 (2017).

[46] T. D. Frazer, J. L. Knobloch, K. M. Hoogeboom-Pot, D. Nardi, W. Chao, R. W. Falcone, M. M. Murnane, H. C. Kapteyn, and J. N. Hernandez-Charpak, Engineering Nanoscale Thermal Transport: Size- and Spacing-Dependent Cooling of Nanostructures, Phys. Rev. Appl. 11, 024042 (2019).

[47] G. Tang, H. H. Yap, J. Ren, and J.-S. Wang, Anomalous Near-Field Heat Transfer in Carbon-Based Nanostructures with Edge States, Phys. Rev. Appl. 11, 031004 (2019).

[48] V. Varshney, S. S. Patnaik, A. K. Roy, G. Froudakis, and B. L. Farmer, Modeling of thermal transport in pillared-graphene architectures, ACS Nano 4, 1153 (2010).

[49] F. Liu, X. Liu, N. Hu, H. Ning, S. Atobe, C. Yan, F. Mo, S. Fu, J. Zhang, Y. Wang, and X. Mu, Investigation of thermal energy transport interface of hybrid graphene-carbon nanotube/polyethylene nanocomposites, Sci. Rep. 7, 14700 (2017).

[50] D. Martinez Gutierrez, A. Di Pierro, A. Pecchia, L. M. Sandonas, R. Gutierrez, M. Bernal, B. Mortazavi, G. Cuniberti, G. Saracco, and A. Fina, Thermal bridging of graphene nanosheets via covalent molecular junctions: A non-equilibrium Green's functions–density functional tight-binding study, Nano Res. 12, 791 (2019).

[51] R. Y. Wang, R. A. Segalman, and A. Majumdar, Room temperature thermal conductance of alkanedithiol self-assembled monolayers, Appl. Phys. Lett. 89, 173113 (2006).

[52] K. Wang, E. Meyhofer, and P. Reddy, Thermal and thermoelectric properties of molecular junctions, Adv. Funct. Mater. 30, 1904534 (2020).

[53] S. Eiamsa-ard and P. Promvonge, Review of Ranque-Hilsch effects in vortex tubes, Renew. Sust. Ener. Rev. 12, 1822 (2008).

[54] S. Subudhi and M. Sen, Review of Ranque-Hilsch vortex tube experiments using air, Renew. Sust. Ener. Rev. 52, 172 (2015).

[55] A. Ameen, *Refrigeration and air Conditioning* (PHI Learning, New Delhi, 2006).

[56] See the Supplemental Material at http://link.aps.org/supplemental/10.1103/PhysRevApplied.15.034008 for additional details on the free-standing and deposited molecular systems.

[57] S. Plimpton, Fast parallel algorithms for short-range molecular dynamics, J. Comp. Phys. 117, 1 (1995).

[58] S. J. Stuart, A. B. Tutein, and J. A. Harrison, A reactive potential for hydrocarbons with intermolecular interactions, J. Chem. Phys. 112, 6472 (2000).

[59] Y. Hu, T. Feng, X. Gu, Z. Fan, X. Wang, M. Lundstrom, S. S. Shrestha, and H. Bao, Unification of nonequilibrium molecular dynamics and the mode-resolved phonon Boltzmann equation for thermal transport simulations, Phys. Rev. B 101, 155308 (2020).

[60] J. Chen, G. Zhang, and B. Li, Molecular dynamics simulations of heat conduction in nanostructures: Effect of heat bath, J. Phys. Soc. Jpn. 79, 074604 (2010).

[61] P. K. Schelling, S. R. Phillpot, and P. Keblinski, Comparison of atomic-level simulation methods for computing thermal conductivity, Phys. Rev. B 65, 144306 (2002).

[62] L. Medrano Sandonas, R. Gutierrez, A. Pecchia, G. Seifert, and G. Cuniberti, Tuning quantum electron and phonon transport in two-dimensional materials by strain engineering: A Green's function based study, Phys. Chem. Chem. Phys. 19, 1487 (2017).

[63] T. Frauenheim, G. Seifert, M. Elsterner, Z. Hajnal, G. Jungnickel, D. Porezag, S. Suhai, and R. Scholz, A self-consistent charge density-functional based tight-binding method for predictive materials simulations in physics, chemistry and biology, Phys. Status Solidi B 217, 41 (2000).

[64] T. Kumagai, S. Izumi, S. Hara, and S. Sakai, Development of bond-order potentials that can reproduce the

elastic constants and melting point of silicon for classical molecular dynamics simulation, Comp. Mater. Sci. **39**, 457 (2007).

[65] M. Neek-Amal and F. M. Peeters, Graphene on boron-nitride: Moiré pattern in the van der Waals energy, Appl. Phys. Lett. **104**, 041909 (2014).

[66] E. P. Bellido and J. M. Seminario, Molecular dynamics simulations of folding of supported graphene, J. Phys. Chem. C **114**, 22472 (2010).

[67] B. Dunweg and W. Paul, Brownian dynamics simulations without Gaussian random numbers, Int. J. Modern Phys. C **02**, 817 (1991).